nature materials

ARTICLES

https://doi.org/10.1038/s41563-019-0422-4

Predictive model of hydrogen trapping and bubbling in nanovoids in bcc metals

Jie Hou[1,2,3,4], Xiang-Shan Kong[1,4], Xuebang Wu[1*], Jun Song[3*] and C. S. Liu[1]

The interplay between hydrogen and nanovoids, despite long being recognized as a central factor in hydrogen-induced damage in structural materials, remains poorly understood. Here, focusing on tungsten as a model body-centred cubic system, we explicitly demonstrate sequential adsorption of hydrogen adatoms on Wigner–Seitz squares of nanovoids with distinct energy levels. Interaction between hydrogen adatoms on nanovoid surfaces is shown to be dominated by pairwise power-law repulsion. We establish a predictive model for quantitative determination of the configurations and energetics of hydrogen adatoms in nanovoids. This model, combined with the equation of states of hydrogen gas, enables the prediction of hydrogen molecule formation in nanovoids. Multiscale simulations, performed based on our model, show good agreement with recent thermal desorption experiments. This work clarifies fundamental physics and provides a full-scale predictive model for hydrogen trapping and bubbling in nanovoids, offering long-sought mechanistic insights that are crucial for understanding hydrogen-induced damage in structural materials.

Hydrogen is the most abundant element in the known universe and is a typical product of corrosion; it thus exists in virtually all service environments. The exposure of metallic materials to hydrogen-rich environments can result in a range of structural damage, including hydrogen-induced cracking[1,2], surface blistering/flaking[3–5] and porosity/swelling[6,7]. This damage undesirably degrades the structural and mechanical integrity of materials[8,9], often causing premature and even catastrophic failure[4,5] and thus jeopardizing the safety and efficiency of many applications. It is generally believed that such damage originates from interactions between hydrogen and various lattice defects. One key issue among those interactions is the interplay between the hydrogen and nanovoids; this promotes the formation and growth of pressurized hydrogen bubbles and consequently leads to experimentally observable failure in structural materials[3–10].

Researchers have long recognized H_2 pressure build-up in a bubble core following cumulative hydrogen adsorption on the bubble surface[11]. However, the accurate characterization of structures, energetics and hydrogen pressure in bubbles has remained lacking. The development of advanced micrographic techniques has enabled the direct observation of hydrogen bubble structures at scales of tens of nanometres[4,10]. However, atomic details of hydrogen bubble nucleation, growth and agglomeration processes are difficult or even impossible to observe in situ. An alternative method to study hydrogen bubble formation is to measure the hydrogen thermal desorption rates during isochronal annealing[12–16], which provides energetic information about hydrogen detrapping from nanovoids in metals. Nevertheless, the hydrogen thermal desorption spectra usually relate to multiple types of crystal defect at different depths[17] and are thus difficult to interpret.

Multiscale simulations provide a way to circumvent such limitations to reveal the missing details[18–20]. The reliability of multiscale results requires accurate characterization of the relevant atomistic behaviour. At the fundamental level, ab initio calculations based on density functional theory (DFT) have been widely used to study the atomistic behaviour of hydrogen in nanovoids[21–37]. Most previous DFT studies have focused only on the simplest case of monovacancies[21–30] and/or divacancies[31–34], with hydrogen empirically placed at high symmetry sites, to investigate the energetic behaviour[21–35]. Recent DFT work[35–37] has tried to extend this method to hydrogen in larger nanovoids by decomposing the nanovoids' inner surfaces into facets of free surfaces, and empirically saturating their high symmetry sites with hard-sphere-like H adatoms. However, this facet approach fails to resolve the inherent structural complexity associated with the highly curved edges and corners in nanovoids, and the hard-sphere approximation is oversimplified to describe just the H–H interaction, thus preventing accurate assessment of the energetics and structures of multiple H atoms in the nanovoids. As well as the above DFT endeavours, notable investigations have been carried out using large-scale classical molecular dynamics (MD) simulations. Vastly different predictions of hydrogen trapping behaviour were obtained depending on the empirical interatomic potentials used[38,39]. Furthermore, many of the available interatomic potentials were fitted as if simulating bulk conditions and cannot reproduce H_2 molecule formation in nanovoids[35,38]; this inherently precludes the ability to predict experimentally observed H_2 pressure build-up in metals[3–5,40–42]. Consequently, it remains difficult to determine which hydrogen trapping behaviours reported, if any, are physically meaningful and/or relevant to hydrogen bubble formation in experiments. The absence of physical models and predictability prevents an accurate analysis of hydrogen behaviour in nanovoids; obtaining mechanistic and multiscale insights into hydrogen bubbling behaviour in metals thus remains a formidable challenge.

The present study aims to directly address the aforementioned challenge. Based on comprehensive first-principles calculations on a model tungsten (W) system, we explicitly demonstrate a sequential adsorption of adatoms on square Wigner–Seitz surfaces of nanovoids with distinct energy levels, and propose a power law to describe the interaction among the H adatoms. A predictive model is established to determine the energetics and stable configurations

[1]Key Laboratory of Materials Physics, Institute of Solid State Physics, Chinese Academy of Sciences, Hefei, China. [2]University of Science and Technology of China, Hefei, China. [3]Department of Mining and Materials Engineering, McGill University, Montreal, Quebec, Canada. [4]These authors contributed equally: Jie Hou, Xiang-Shan Kong. *e-mail: xbwu@issp.ac.cn; jun.song2@mcgill.ca

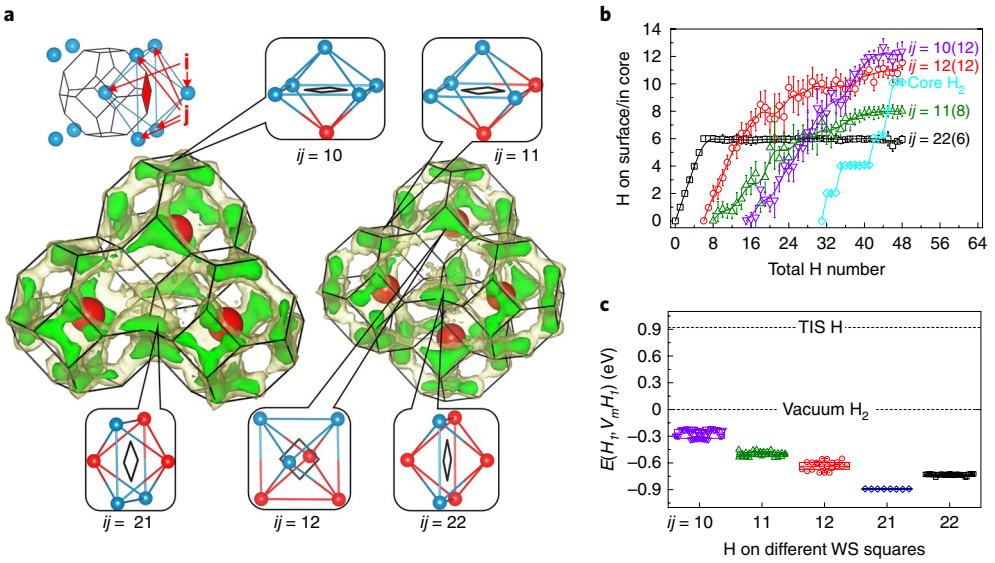

Fig. 1 | Characterization of nanovoid surfaces and related hydrogen energy levels. a, H probability density isosurfaces (in green and yellow) in V_3 and V_4 nanovoids during hydrogen addition at 600 K. Blue and red spheres, metal and vacancy sites, respectively; black lines, edges of the Wigner–Seitz cells; *i*,*j*, vacancy numbers of two types of neighbouring metal site around a Wigner–Seitz square. W atoms (not shown) are fixed at their ideal bcc sites. **b**, Average H numbers on different Wigner–Seitz squares (as adatoms) or in the core (as molecules) in V_8 at 600 K. Shown in parentheses are the numbers of corresponding Wigner–Seitz squares on the V_8 surface (note, V_8 does not contain $ij = 21$ Wigner–Seitz squares; see Supplementary Table 1). Error bars show s.d. of the data; lines are guides to the eye. **c**, Trapping energy of a single H adatom (that is, $E(H_1, V_mH_1)$, see equation (1)) on all symmetrically irreducible Wigner–Seitz (WS) squares in V_1–V_8, distributed using a standard boxplot. Lines marked as 'TIS H' and 'Vacuum H_2' represent a H atom at the tetrahedral interstitial site in the bulk metal lattice and in a H_2 molecule in vacuum, respectively. Additional results for other nanovoids are provided in Supplementary Section 1.

of multiple H adatoms in nanovoids. Combined with the equation of state of pressurized H_2, this model enables quantitative assessment of the competition between H adatoms and H_2 molecules, as well as the prediction of pressurized H_2 molecule formation in nanovoids. Multiscale simulations based on the model show very good agreement with recent deuterium (D) thermal desorption experiments. The generality of our approach and model is further confirmed by benchmark calculations on other typical body-centred cubic (bcc) metals (Mo, Cr and α-Fe). The present study clarifies the fundamental physical rules of hydrogen trapping and bubbling in general nanovoids in bcc metals, provides the long-sought predictability for guiding related experiments as well as benchmarks for developing new metal–H empirical interatomic potentials, and enables a critical step towards quantitative assessment of hydrogen-induced damage in materials.

Structures of H adatoms trapped in nanovoids

The general patterns of hydrogen trapping in nanovoids were examined by comprehensive ab initio MD simulations. H atoms were sequentially introduced into a nanovoid (V_m) to form H–nanovoid clusters (V_mH_n), where $m \approx 1$–8 and $n \geq 0$ respectively denote the number of vacancies constituting the nanovoid and the number of H atoms enclosed therein. As with previous studies[36,37], we observed H adatom adsorption on the surfaces of all nanovoids and H_2 molecule formation in the core of large nanovoids (V_mH_n with $m \geq 3$), evidenced by two distinct pairing states with H–H separation distances of ~1.94 and 0.75 Å, respectively (Supplementary Section 1).

Figure 1a illustrates the spatial locations of regions of high H probability density (that is, the probability of finding a H atom in a unit volume) in nanovoids during hydrogen addition. Our results indicate that the H adatoms prefer to stay on the square surfaces of the Wigner–Seitz cells of nanovoids (in the following, these square units are referred to as Wigner–Seitz squares), in particular near their vertices (that is, the tetrahedral interstitial sites). As shown in Fig. 1a, each Wigner–Seitz square is enclosed by six metal sites. Other metal sites are more than 2.9 Å away from the H adatoms on the Wigner–Seitz square, significantly greater than the typical transition metal–H bond length (1.5–2 Å)[43]. It is thus reasonable to assume that the energetic behaviour of H adatoms on a Wigner–Seitz square are mainly influenced by these six metal sites enclosing the square[22]. For a Wigner–Seitz square on a nanovoid surface, note that parts of these six metal sites are occupied by vacancies. Consequently, the complex nanovoid surface can be categorized into five different Wigner–Seitz squares, with *i* and *j* denoting the vacancy numbers of two types of neighbouring metal site (Fig. 1a). Figure 1b presents an example of the average number of H atoms on each type of Wigner–Seitz square obtained from ab initio MD simulations. Despite certain temperature-induced fluctuation (at a relatively high temperature of 600 K), these show that H adatoms sequentially occupy different types of Wigner–Seitz square (for example, in the order $ij = 22$, 12, 11, 10 in Fig. 1b) until all squares are filled. After a certain prerequisite surface trapping, H_2 molecules begin to form in the core of large nanovoids ($V_{\geq 3}$) (Supplementary Section 1). This spatial preference clearly indicates an energy difference among H on different Wigner–Seitz squares and H_2 in the core.

To quantitatively analyse the energetics of hydrogen, we define the trapping energy of a number k of H atoms ($k \leq n$) in a V_mH_n cluster as

$$E(H_k, V_mH_n) = E^{\mathrm{tot}}(V_mH_n) - E^{\mathrm{tot}}(V_mH_{n-k}) - \frac{k}{2}E^{\mathrm{tot}}(H_2) \quad (1)$$

where $E^{\mathrm{tot}}(V_mH_{n-k})$ and $E^{\mathrm{tot}}(V_mH_n)$ are the total energies of the reference metal matrix containing the stable V_mH_{n-k} and V_mH_n clusters, respectively, before and after the introduction of k H atoms,

and $E^{tot}(H_2)$ is the total energy of an isolated H_2 molecule in vacuum (with a bond energy of 4.56 eV). First, we consider the case of nanovoids containing a single H adatom; the calculated trapping energies of hydrogen (that is, $E(H_1,V_mH_1)$ with $m \approx 1$–8) are shown in Fig. 1c. We find that those trapping energies can be nicely categorized by the five different types of Wigner–Seitz square where the hydrogen resides after relaxation, accordingly falling into five distinct energy levels. These energy levels are insensitive to nanovoid size, which confirms the previous assumption that the hydrogen energetics on a Wigner–Seitz square are only affected by the six metal sites enclosing the square. Figure 1c shows the energetic preference of a H adatom on different Wigner–Seitz squares; this is in close accordance with the occupancy preference (Fig. 1b) obtained from the ab initio MD simulations.

Interaction between H adatoms

After clarifying the distinct energy level of a single H adatom in a nanovoid (that is, V_mH_1), we further investigated the energetics of multiple H atoms in the nanovoids. In the following, we first assume that the H atoms stay in the form of adatoms for simplicity of analysis. The mutual interaction between H adatoms in nanovoids can be quantified by defining the H–H interaction energy:

$$E^{int}(V_mH_n) = E^{tot}(V_mH_n) + (n-1)E^{tot}(V_m) - \sum_{k=1}^{n} E^{tot}(V_mH_1^{S_k}) \quad (2)$$

where S_1, S_2, …, S_n indicate the sites of the n H adatoms in the V_mH_n cluster, and $E^{tot}(V_mH_1^{S_k})$ represents the total energy of the reference metal matrix containing a $V_mH_1^{S_k}$ cluster with the H adatom located at the S_k site.

To unravel the complex H–H interaction, we started by examining nanovoids containing two H adatoms, that is, V_mH_2. Figure 2a shows the corresponding pairwise H–H interaction $E^{int}(V_mH_2)$, from which we see that the H–H interaction is generally repulsive and decays rapidly as the H–H separation distance d increases. Intriguingly, we found that the pairwise H–H interaction on a nanovoid surface can be well described by a d^{-5} power law, similar to that for hydrogen on free metal surfaces[44]:

$$E^{int}(V_mH_2) = A_s d^{-5} \quad (3)$$

where $A_s = 3.19$ eV Å^5 is a fitted constant. As a consequence of this strong repulsion, it is expected that H adatoms would shift towards tetrahedral interstitial sites on Wigner–Seitz squares to increase the H–H separation distances on adding hydrogen, consistent with Fig. 1a, which shows high H probability at tetrahedral interstitial sites. Also, a Wigner–Seitz square would prefer to accommodate only one H adatom until all other Wigner–Seitz squares are occupied by H adatom(s), which is in line with the results presented in Fig. 1b.

Energetics of H adatoms in nanovoids

For the general case of V_mH_n (with $n \geq 2$), according to our definition of the H–H interaction energy (equation (2)), the overall trapping energy of the n number of H adatoms in V_mH_n can be rewritten as

$$E(H_n, V_mH_n) = \sum_{k=1}^{n} E(H_1, V_mH_1^{S_k}) + E^{int}(V_mH_n) \quad (4)$$

If we assume that the H–H interaction, $E^{int}(V_mH_n)$, remains pairwise in nature and described by the same d^{-5} law as in equation (3), we can then represent the overall trapping energy as

$$E(H_n, V_mH_n) \cong \sum_{k=1}^{n} E_k^{ij} + A_s \sum_{k<1}^{n} d_{kl}^{-5} \quad (5)$$

where d_{kl} denotes the distance between two H adatoms at S_k and S_l sites, respectively. As previously demonstrated (Fig. 1c), $E(H_1, V_mH_1^{S_k})$ in equation (4) would conform to one of the five energy levels, being directly prescribed by the Wigner–Seitz square where site S_k is located, denoted as E_k^{ij}.

To verify equation (5), we calculated the trapping energies for V_mH_n clusters (note that these clusters contain only H adatoms with no H_2 molecule formation, in order to limit the focus to H adatoms). We screened different candidate structures: (1) selected randomly from the ab initio MD trajectories (15 structures for each V_mH_n), (2) constructed by manually adding H on Wigner–Seitz squares with the lowest energy level, and (3) constructed by adjusting the H position to minimize the trapping energy given by equation (5). In most cases, we found that the minimizing equation (5) method could identify the structures with the lowest energies. In Fig. 2b we also show that the interaction energy among multiple H adatoms can be estimated well by summing up pairwise d^{-5} interactions, that is, the adatom interaction term in equation (5). More importantly, as demonstrated in Fig. 2c, the overall trapping energies $E(H_n, V_mH_n)$ predicted by equation (5) are in close agreement with DFT data. These results clearly show that equation (5) captures the physical essence of multiple H adsorption on nanovoid surfaces, providing a simple but effective framework for determining the stable structures of multiple H adatoms in nanovoids.

Equation (5) allows us to predict hydrogen trapping energies for any V_mH_n cluster based on H structures. However, DFT relaxations are still indispensable for determining accurate H adatom sites and their mutual separation, which makes equation (5) less practical. To simplify the problem, yet without losing physical generality, two approximations are introduced here based on the DFT results: (1) H adatoms sequentially fill Wigner–Seitz squares with the lowest energy, and are uniformly distributed on the surface to maximize H–H distances; (2) each H adatom has six nearest H neighbours (that is, close-packed distribution), and interactions between non-nearest adatoms are neglected considering the d^{-5} rapid decay. In this way, the nearest H–H distance is $d = \left(\frac{2a}{\sqrt{3}n}\right)^{0.5}$, where a is the surface area of the nanovoid. Consequently, the multiple H–H interaction energy, that is, the second term in the right side of equation (4), can be simplified to

$$E^{int}(V_mH_n) \cong \frac{1}{2} A_s 6n \left(\frac{\sqrt{3}n}{2a}\right)^{2.5} \quad (6)$$

According to equations (1), (5) and (6), the trapping energy of the nth H adatom in a V_mH_n cluster is given by

$$E(H_1, V_mH_n) = E_k^{ij} + \frac{\partial E^{int}(V_mH_n)}{\partial n} \cong E_k^{ij} + 7.3A_s \left(\frac{n}{a}\right)^{2.5} \quad (7)$$

Additional details related to the above are provided in Supplementary Section 2. Equation (7) provides a quantitative prediction of the trapping energies of H adatoms just simply knowing the surface H density, n/a. The predictions from equation (7) in Fig. 3 (blue lines) show consistent agreement with the DFT-calculated trapping energies. This confirms the validity of the two approximations in describing the general behaviour of H adatoms in nanovoids. One particular observation in Fig. 3 is that the hydrogen trapping energy generally exhibits a combination of stepwise increments and gradual climbing. The stepwise growth is related to distinct energy levels (that is, different E_n^{ij}), corresponding to H occupying different types of Wigner–Seitz square (Fig. 1). Meanwhile, the gradual climbing in the trapping energy

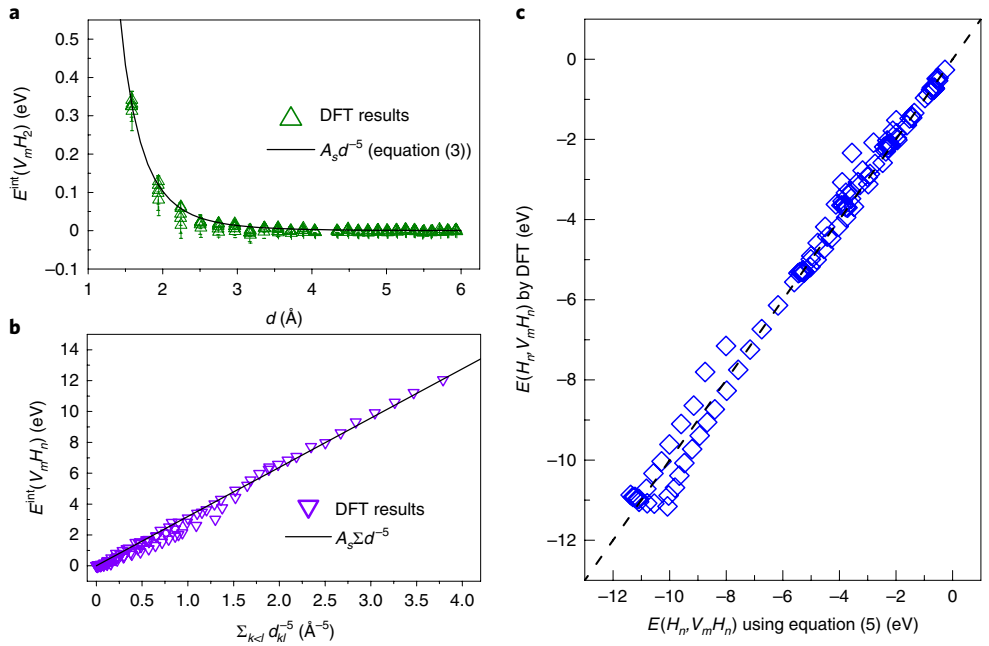

Fig. 2 | Energetics of H adatoms on nanovoid surfaces. a, Pairwise H–H interaction energies in different nanovoids. Symbols are DFT data calculated using equation (2), solid lines are fits using the d^{-5} power function, where d is the separation distance between two H adatoms at different tetrahedral interstitial sites, averaged among all symmetrically irreducible H–H pairs, with error bars showing s.d. of the data. **b**, Interaction energies among multiple H adatoms in the most stable V_mH_n clusters as a function of the sum of pairwise d^{-5}. **c**, Comparison of overall trapping energies from DFT calculations (symbols) and those predicted by equation (5) (dashed line).

results from the decreasing H–H distance and thus the increasing H–H repulsion. As H adatoms continue to populate the nanovoid, eventually the trapping energy will reach the value of an interstitial H in a bulk metal lattice, $E^{H}_{Bulk} = 0.92$ eV, when the nanovoid surface will be fully saturated, namely the surface H density reaches its maximum. Under such a condition, E_n^{ij} will assume the highest energy level, that is, $E_n^{ij=10}$ (Fig. 1c), and the maximum density can be calculated (by $E(H_1, V_mH_n) = E^{H}_{Bulk}$) to be 0.304 H Å^{-2}, corresponding to a nearest-neighbouring H–H distance of 1.95 Å, in line with the H–H pairing state (1.94 Å, Supplementary Section 1) observed in ab initio MD simulations.

H_2 molecule formation in nanovoids

In our above analysis, H atoms are assumed to stay in nanovoids in the form of adatoms. However, as seen in Fig. 3, with the continuous introduction of H atoms into a nanovoid, the trapping energy of the H adatom becomes positive, suggesting the possibility of H_2 molecule formation. Indeed, H_2 molecule formation has been noted in DFT calculations in large nanovoids (shown as filled symbols in Fig. 3). In Fig. 3, we also note that, along with the formation of H_2 molecules, a notable deviation between the predictions (of H trapping energies) from equation (7) and the DFT data appears. This deviation is understandable, as equation (7) is only applicable for describing H adatoms. To remedy the discrepancy, we need to account for H_2 molecule formation in our model. H_2 molecules in the nanovoid core can be characterized by the equation of states as (for details see Supplementary Section 2)

$$p = A_c\left(\frac{n_c}{v}\right)^3$$

where p is pressure, v is the core volume of the nanovoid, n_c is twice the number of H_2 molecules presented in the nanovoid and $A_c = 8.01$ eV Å^6 is a constant that fits well to both the experimental[45,46] and our DFT results. The trapping energies corresponding to molecular hydrogen in the nanovoid core can be expressed by

$$E(H_1, V_mH_{n_c}) = \int_0^p \left(\frac{\partial v}{\partial n_c}\right)_P \mathrm{d}P = \frac{3}{2}A_c\left(\frac{n_c}{v}\right)^2 \quad (8)$$

which depends on volumetric H density, n_c/v, in the nanovoid core. Denoting the number of H adatoms on the nanovoid surface as n_s, we have the total number of H atoms in the nanovoid $n = n_s + n_c$. Combining equations (7) and (8), we can determine the partitioning of the hydrogen into the adatom and molecule states as

$$E(H_1, V_mH_n) = \frac{3}{2}A_c\left(\frac{n_c}{v}\right)^2 = E_{n_s}^{ij} + 7.3A_s\left(\frac{n_s}{a}\right)^{2.5} \quad (9)$$

From the above, the further evolution of hydrogen trapping energy in the event of H_2 molecule formation can then be obtained, as illustrated by the red curves in Fig. 3. We see that this new model prediction yields very good agreement with the DFT data for the regime of hydrogen trapping energy being positive. Moreover, the above framework can be readily extended to hydrogen bubbling in a nanovoid at finite temperatures and under varying chemical environments, by equating the chemical potential of hydrogen in the nanovoid core, μ^{H}_{core}, with that of bulk hydrogen, μ^{H}_{B}:

$$\mu^{H}_{core} = \int_0^p \left(\frac{\partial v}{\partial n_c}\right)_P \mathrm{d}P = \mu^{H}_{B} = E^{H}_{Bulk} + k_B T \ln\left(\frac{C_H}{1-C_H}\right) \quad (10)$$

where k_B is Boltzmann's constant, T denotes the temperature, C_H is the bulk H concentration and E^{H}_{Bulk} (=0.92 eV) is the trapping energy of the H interstitial in a bulk W lattice. Note that the equation of states for high-pressure H_2 is relatively insensitive to temperature[47]. Consequently, combining equations (8) and (10), the

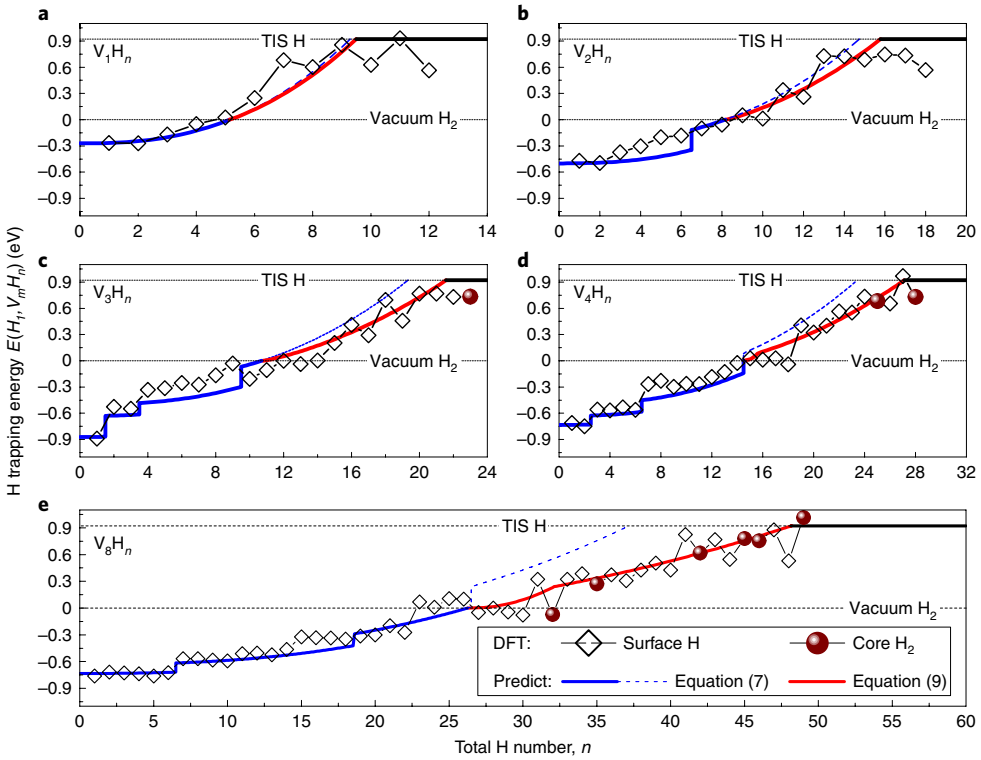

Fig. 3 | Comparison between model predictions and DFT results. a–e, H trapping energy as a function of total H number in V_1–V_4 (**a**–**d**) and V_8 (**e**) nanovoids. DFT results are shown using open (for H adatoms) and filled (when forming a new H_2 molecule) symbols. Blue lines, model predictions given by equation (7); red lines, predictions given by equation (9). Lines marked 'TIS H' and 'Vacuum H_2' represent a H atom at the tetrahedral interstitial site in a bulk metal lattice and in a H_2 molecule in vacuum, respectively.

hydrogen bubbling pressure under thermodynamic equilibrium can be obtained as

$$p = \frac{1}{\sqrt{A_c}}\left[\frac{2}{3}\left(E^{H}_{Bulk} + k_B T \ln\left(\frac{C_H}{1-C_H}\right)\right)\right]^{\frac{3}{2}} \quad (11)$$

which solely depends on temperature, concentration and the energy state of hydrogen in the bulk lattice. With high hydrogen concentration and low temperature, the bubble pressure can be high enough to induce spontaneous bubble growth via mechanisms like loop-punching (Supplementary Section 4).

Model verification and application

The good agreement between the model prediction and DFT data (Figs. 2 and 3) provides evidence that our model captures the fundamental physics underlying hydrogen trapping and interaction in nanovoids. It is important to note that the model parameters E_n^{ij}, A_s and A_c are not sensitive to the size or configuration of the nanovoid, and thus the model is readily applicable to larger systems and for examining hydrogen bubble formation. Furthermore, preliminary calculations have been performed for Mo, Cr and α-Fe systems and similar hydrogen behaviour has been demonstrated (Supplementary Fig. 8), confirming the generality of our model for application in other bcc metals.

The proposed model accurately predicts hydrogen trapping configurations, hydrogen energetics and H_2 molecule formation in nanovoids, with a finite set of DFT calculations. Such predictions may serve as critical benchmarks for developing new metal–H empirical interatomic potentials for classical MD simulations (Supplementary Section 4). Meanwhile they provide atomic-precision data to feed into large-scale methods such as kinetic Monte Carlo simulations[48], enabling a multiscale approach that directly bridges atomistic data with macroscopic experiments. In the following, we present one typical example comparing recent deuterium thermal desorption spectroscopy (TDS) results[12,13], which determine the energetic information regarding deuterium trapping in nanovoids experimentally, with our predictive model based multiscale simulations. In these two TDS experiments, irradiation-damaged W samples were treated by annealing procedures at 550 and 800 K, respectively. With vacancies being mobile only above 550 K (refs. [49,50]), it is postulated[12,13] that these two annealing temperatures would render irradiation-induced defects in W samples as small and large nanovoids, respectively. These annealed samples were subsequently implanted with low-energy D ions, followed by TDS measurements at different heating rates. The TDS spectra data corresponding to radiation defects (reproduced from refs. [12,13]) are shown in Fig. 4.

Combining our predictive model, primary irradiation damage simulations and an object kinetic Monte Carlo method, we carried out multiscale simulations to reproduce and interpret the experimental TDS results (for details see Supplementary Section 4). To make a direct comparison, the same irradiation and annealing conditions as those used in the experimental studies[12,13] were used in the simulations. As seen in Fig. 4, the simulated TDS curves (lines) match the experimental results (symbols) well for the temperature range in which the H–nanovoid interaction dominates. In particular, the simulated desorption peaks in Fig. 4a correspond to D release from small nanovoids (mostly V_1–V_2), while the desorption peaks in Fig. 4b are attributed to large nanovoids (mostly V_6–V_{15}), confirming the experimental speculations[12,13]. Aside from some minor discrepancies at low temperatures, which may be contributed by other defects like dislocations or grain boundaries[12,13], our simulations accurately reproduce the experimental observations.

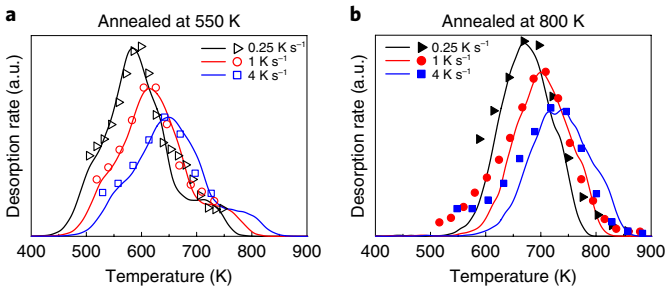

Fig. 4 | Thermal desorption spectra of deuterium from W. a,**b**, Samples were irradiated at 10 keV per D ion to a fluence of 3×10^{19} D m^{-2}, annealed at 550 K (**a**) and 800 K (**b**) for 5 min to render small and large nanovoids, implanted with 0.67 keV per D ions to a fluence of 10^{19} D m^{-2}, then annealed at different heating rates. Lines are multiscale modelling results and symbols are experimental data from refs. [12] (open) and [13] (filled).

In summary, the present study explicitly demonstrates sequential adsorption of H adatoms on Wigner–Seitz squares of nanovoids with distinct energy levels, based on comprehensive first-principles calculations using W as a representative bcc system. A power law has been demonstrated and verified to accurately describe the interaction between H adatoms within nanovoids. This study clarifies fundamental physical rules governing hydrogen trapping, interaction and bubbling in nanovoids in bcc metals. A comprehensive modelling framework has been established to enable accurate predictions of hydrogen energetics and H_2 molecule formation in nanovoids. Our study offers the long-sought mechanistic insights crucial for understanding hydrogen-induced damage in structural materials, and provides essential predictive tools for developing new H–metal interatomic potentials, and multiscale modelling of hydrogen bubble nucleation and growth.

Online content

Any methods, additional references, Nature Research reporting summaries, source data, statements of code and data availability and associated accession codes are available at https://doi.org/10.1038/s41563-019-0422-4.

Received: 5 September 2018; Accepted: 5 June 2019;
Published online: 15 July 2019

References

1. Zhang, Z., Obasi, G., Morana, R. & Preuss, M. Hydrogen assisted crack initiation and propagation in a nickel-based superalloy. *Acta Mater.* **113**, 272–283 (2016).
2. Song, J. & Curtin, W. A. Atomic mechanism and prediction of hydrogen embrittlement in iron. *Nat. Mater.* **12**, 145–151 (2013).
3. Tiegel, M. C. et al. Crack and blister initiation and growth in purified iron due to hydrogen loading. *Acta Mater.* **115**, 24–34 (2016).
4. Xie, D. G. et al. In situ study of the initiation of hydrogen bubbles at the aluminium metal/oxide interface. *Nat. Mater.* **14**, 899–903 (2015).
5. Jia, Y. Z. et al. Subsurface deuterium bubble formation in W due to low-energy high flux deuterium plasma exposure. *Nucl. Fusion* **57**, 034003 (2017).
6. Garner, F. A. et al. Retention of hydrogen in fcc metals irradiated at temperatures leading to high densities of bubbles or voids. *J. Nucl. Mater.* **356**, 122–135 (2006).
7. Toda, H. et al. Growth behavior of hydrogen micropores in aluminum alloys during high-temperature exposure. *Acta Mater.* **57**, 2277–2290 (2009).
8. Neeraj, T., Srinivasan, R. & Li, J. Hydrogen embrittlement of ferritic steels: observations on deformation microstructure, nanoscale dimples and failure by nanovoiding. *Acta Mater.* **60**, 5160–5171 (2012).
9. Robertson, I. M. et al. Hydrogen embrittlement understood. *Metall. Mater. Trans. B* **46**, 1085–1103 (2015).
10. Zhao, J. et al. Investigation of hydrogen bubbles behavior in tungsten by high-flux hydrogen implantation. *J. Nucl. Mater.* **503**, 198–204 (2018).
11. Veen, A. V. et al. Hydrogen exchange with voids in tungsten observed with TDS and PA. *J. Nucl. Mater.* **155–157**, 1113–1117 (1988).
12. Zibrov, M., Ryabtsev, S., Gasparyan, Y. & Pisarev, A. Experimental determination of the deuterium binding energy with vacancies in tungsten. *J. Nucl. Mater.* **477**, 292–297 (2016).
13. Ryabtsev, S., Gasparyan, Y., Zibrov, M., Shubina, A. & Pisarev, A. Deuterium thermal desorption from vacancy clusters in tungsten. *Nucl. Instrum. Methods Phys. Res. B* **382**, 101–104 (2016).
14. Ogorodnikova, O. V. et al. Surface modification and deuterium retention in reduced-activation steels under low-energy deuterium plasma exposure. Part II: Steels pre-damaged with 20 MeV W ions and high heat flux. *Nucl. Fusion* **57**, 036011 (2017).
15. Zhu, X.-L. et al. Deuterium occupation of vacancy-type defects in argon-damaged tungsten exposed to high flux and low energy deuterium plasma. *Nucl. Fusion* **56**, 036010 (2016).
16. Ogorodnikova, O. V., Roth, J. & Mayer, M. Ion-driven deuterium retention in tungsten. *J. Appl. Phys.* **103**, 034902 (2008).
17. Guterl, J., Smirnov, R. D., Krasheninnikov, S. I., Zibrov, M. & Pisarev, A. A. Theoretical analysis of deuterium retention in tungsten plasma-facing components induced by various traps via thermal desorption spectroscopy. *Nucl. Fusion* **55**, 093017 (2015).
18. Fu, C.-C., Torre, J. D., Willaime, F., Bocquet, J.-L. & Barbu, A. Multiscale modelling of defect kinetics in irradiated iron. *Nat. Mater.* **4**, 68–74 (2004).
19. Valles, G. et al. Influence of grain boundaries on the radiation-induced defects and hydrogen in nanostructured and coarse-grained tungsten. *Acta Mater.* **122**, 277–286 (2017).
20. De Backer, A. et al. Multiscale modelling of the interaction of hydrogen with interstitial defects and dislocations in bcc tungsten. *Nucl. Fusion* **58**, 016006 (2018).
21. Liu, Y.-L., Zhang, Y., Zhou, H.-B. & Lu, G.-H. Vacancy trapping mechanism for hydrogen bubble formation in metal. *Phys.Rev. B* **79**, 172103 (2009).
22. Xing, W. et al. Unified mechanism for hydrogen trapping at metal vacancies. *Int. J. Hydrog. Energy* **39**, 11321–11327 (2014).
23. Ohsawa, K., Goto, J., Yamakami, M., Yamaguchi, M. & Yagi, M. Trapping of multiple hydrogen atoms in a tungsten monovacancy from first principles. *Phys. Rev. B* **82**, 184117 (2010).
24. Ohsawa, K., Eguchi, K., Watanabe, H., Yamaguchi, M. & Yagi, M. Configuration and binding energy of multiple hydrogen atoms trapped in monovacancy in bcc transition metals. *Phys. Rev. B* **85**, 094102 (2012).
25. You, Y.-W. et al. Dissolving, trapping and detrapping mechanisms of hydrogen in bcc and fcc transition metals. *AIP Adv.* **3**, 012118 (2013).
26. Tanguy, D., Wang, Y. & Connétable, D. Stability of vacancy-hydrogen clusters in nickel from first-principles calculations. *Acta Mater.* **78**, 135–143 (2014).
27. Gui, L.-J. et al. First-principles investigation on vacancy trapping behaviors of hydrogen in vanadium. *J. Nucl. Mater.* **442**, S688–S693 (2013).
28. Kong, X.-S. et al. First-principles calculations of hydrogen solution and diffusion in tungsten: temperature and defect-trapping effects. *Acta Mater.* **84**, 426–435 (2015).
29. Fernandez, N., Ferro, Y. & Kato, D. Hydrogen diffusion and vacancies formation in tungsten: density functional theory calculations and statistical models. *Acta Mater.* **94**, 307–318 (2015).
30. Ismer, L., Park, M. S., Janotti, A. & Van de Walle, C. G. Interactions between hydrogen impurities and vacancies in Mg and Al: a comparative analysis based on density functional theory. *Phys. Rev. B* **80**, 184110 (2009).
31. Tateyama, Y. & Ohno, T. Stability and clusterization of hydrogen-vacancy complexes in α−Fe: an ab initio study. *Phys. Rev. B* **67**, 174105 (2003).
32. You, Y.-W. et al. Clustering of H and He, and their effects on vacancy evolution in tungsten in a fusion environment. *Nucl. Fusion* **54**, 103007 (2014).
33. Lu, G. & Kaxiras, E. Hydrogen embrittlement of aluminum: the crucial role of vacancies. *Phys. Rev. Lett.* **94**, 155501 (2005).
34. Monasterio, P. R., Lau, T. T., Yip, S. & Van Vliet, K. J. Hydrogen-vacancy interactions in Fe–C alloys. *Phys. Rev. Lett.* **103**, 085501 (2009).
35. Hayward, E. & Fu, C.-C. Interplay between hydrogen and vacancies in α-Fe. *Phys. Rev. B* **87**, 174103 (2013).
36. Hayward, E., Hayward, R. & Fu, C.-C. Predicting distinct regimes of hydrogen behavior at nano-cavities in metals. *J. Nucl. Mater.* **476**, 36–44 (2016).
37. Geng, W. T. et al. Hydrogen bubble nucleation in α-iron. *Scripta Mater.* **134**, 105–109 (2017).
38. Wang, L. F., Shu, X., Lu, G. H. & Gao, F. Embedded-atom method potential for modeling hydrogen and hydrogen–defect interaction in tungsten. *J. Phys. Condens. Matter* **29**, 435401 (2017).
39. Cusentino, M. A., Hammond, K. D., Sefta, F., Juslin, N. & Wirth, B. D. A comparison of interatomic potentials for modeling tungsten–hydrogen–helium plasma–surface interactions. *J. Nucl. Mater.* **463**, 347–350 (2015).
40. Brimbal, D. et al. Application of Raman spectroscopy to the study of hydrogen in an ion irradiated oxide-dispersion strengthened Fe–12Cr steel. *J. Nucl. Mater.* **447**, 179–182 (2014).
41. Koch, S. J., Lavrov, E. V. & Weber, J. Towards understanding the hydrogen molecule in ZnO. *Phys. Rev. B* **90**, 205212 (2014).

42. van de Walle, C. G. & P.Goss, J. Energetics and vibrational frequencies of interstitial H_2 molecules in semiconductors. *Mater. Sci. Eng. B* **58**, 17–23 (1999).
43. Christmann, K. Interaction of hydrogen with solid surfaces. *Surf. Sci. Rep.* **9**, 1–163 (1988).
44. Einstein, T. L. in *Handbook of Surface Science* Vol. 1, 1st edn (ed. Unertl, W. N.) Ch. 11 (Elsevier, 1996).
45. Loubeyre, P. et al. X-ray diffraction and equation of state of hydrogen at megabar pressures. *Nature* **383**, 702–704 (1996).
46. Shimizu, H. & Brody, E. M. Brillouin measurements of solid n-H_2 and n-D_2 to 200 kbar at room temperature. *Phys. Rev. Lett.* **47**, 128–131 (1981).
47. Hemmes, H., Driessen, A. & Griessen, R. Thermodynamic properties of hydrogen at pressures up to 1 Mbar and temperatures between 100 and 1000 K. *J. Phys. C* **19**, 3571–3585 (1986).
48. Becquart, C. S., Domain, C., Sarkar, U., DeBacker, A. & Hou, M. Microstructural evolution of irradiated tungsten: ab initio parameterisation of an OKMC model. *J. Nucl. Mater.* **403**, 75–88 (2010).
49. Debelle, A., Barthe, M. F. & Sauvage, T. First temperature stage evolution of irradiation-induced defects in tungsten studied by positron annihilation spectroscopy. *J. Nucl. Mater.* **376**, 216–221 (2008).
50. De Backer, A., Lhuillier, P. E., Becquart, C. S. & Barthe, M. F. Modelling of the implantation and the annealing stages of 800keV ^{3}He implanted tungsten: formation of nanovoids in the near surface region. *J. Nucl. Mater.* **429**, 78–91 (2012).

Acknowledgements

The authors thank Y. Li at the Institute of Solid State Physics, Chinese Academy of Sciences for providing the IM3D primary irradiation damage data. The authors are grateful for valuable comments and discussion from G. Lu at Beihang University and W. Han at Xi'an Jiaotong University, and also thank G. Lu for providing the empirical-potential-based hydrogen trapping data from his earlier work. This work was financially supported by the National Magnetic Confinement Fusion Energy Research Project (grant no. 2015GB112001), the National Key R&D Program of China (grant no. 2018YFE0308102), the National Natural Science Foundation of China (nos. 11735015, 51771185 and 11575229) and the Natural Sciences and Engineering Research Council of Canada Discovery grant no. RGPIN-2017-05187. J.H. acknowledges financial support from the China Scholarship Council (CSC). J.H. and J.S. acknowledge the Supercomputer Consortium Laval UQAM McGill and Eastern Quebec for providing computing resources. X.W. acknowledges support from the Youth Innovation Promotion Association of CAS (2015384).

Author contributions

J.S. and X.W. conceived the original idea and designed the work. X.S.K. and J.H. conducted the simulations with help from C.S.L. All authors wrote the paper and discussed the results. C.S.L. and J.S. supervised the project.

Competing interests

The authors declare no competing interests.

Additional information

Supplementary information is available for this paper at https://doi.org/10.1038/s41563-019-0422-4.

Reprints and permissions information is available at www.nature.com/reprints.

Correspondence and requests for materials should be addressed to X.W. or J.S.

Publisher's note: Springer Nature remains neutral with regard to jurisdictional claims in published maps and institutional affiliations.

Methods

First-principles DFT calculations. First-principles DFT calculations were performed using the Vienna ab initio simulation package (VASP)[51,52] with Blöchl's projector augmented wave (PAW) potential method[53]. All the 5*d* and 6*s* electrons of the metal and the 1*s* electron of H were treated as valence electrons. The exchange-correlation energy functional was described with the generalized gradient approximation (GGA) as parameterized by Perdew–Wang (PW91)[54,55]. A super-cell containing 128 lattice points (4×4×4 duplicate of a conventional bcc unit cell) was used in the calculations.

Nanovoids were constructed with stable structures obtained from a previous DFT study[56]. Relaxation of the atomic positions and super-cell shapes and sizes was performed for all calculations, except for those examining the pairwise H–H interaction, where all atoms were fixed to avoid H–H separation adjustment during relaxation. The convergence criteria for energy and atomic force were set as 10^{-6} eV and 0.01 eV Å^{-1}, respectively. A 500 eV plane wave cutoff and a 3×3×3 *k*-point grid obtained using the Monkhorst–Pack method[51] were used. Benchmark calculations with increased super-cell size, cutoff energy, *k*-point density as well as with zero-point energy correction for H were carried out, and a negligible influence on our results was found (Supplementary Section 5). Moreover, benchmark investigation of hydrogen in meta-stable nanovoid configurations was also performed and very similar behaviour (energy levels and H–H interaction) was verified (Supplementary Section 5).

Ab initio MD simulations. Ab initio MD simulations were performed in the canonical (NVT) ensemble with a Nose–Hoover thermostat using the VASP code. A lower cutoff energy (350 eV) and a 1×1×1 *k*-point grid were adopted. The Verlet algorithm was used for integration of Newton's equations of motion. All systems were simulated at 600 K with a time step of 1 fs. H atoms were randomly added into nanovoids at a rate of 1 atom per 5 ps. To avoid the potential influence of the initial hydrogen addition positions, the results for the first 2 ps after each H addition were excluded from the spatial distribution analysis.

Multiscale simulations. Thermal desorption spectra of the hydrogen isotopes were simulated by a quantitative multiscale modelling approach, which incorporates atomistic scale H–nanovoid interactions, irradiation-induced primary damages and large-scale object kinetic Monte Carlo (OKMC) simulations. General algorithms of the OKMC method and parameterizations of defects are described in detail elsewhere[28,48,57,58]. A 60×60×500 nm^3 box was used in all OKMC simulations, with periodic boundary conditions applied on the first two dimensions and hydrogen allowed to desorb at the surface of the third dimension. Interactions between the hydrogen and nanovoids were parameterized using the predictive model conveyed by equation (9). Primary irradiation damage databases were tabulated using the binary collision Monte Carlo code IM3D[59], and invoked during OKMC simulations of D. The kinetic energies of D, irradiation fluxes, irradiation time and temperatures were calibrated according to the corresponding experimental conditions[12].

Data availability

The data generated and/or analysed within the current study will be made available upon reasonable request to the authors.

Code availability

The code for the object kinetic Monte Carlo simulations will be made available upon reasonable request to the authors.

References

51. Kresse, G. & Hafner, J. Ab initio molecular dynamics for open-shell transition metals. *Phys. Rev. B* **48**, 13115–13118 (1993).
52. Kresse, G. & Hafner, J. Ab initio molecular dynamics for liquid metals. *Phys. Rev. B* **47**, 558–561 (1993).
53. Blöchl, P. E. Projector augmented-wave method. *Phys. Rev. B* **50**, 17953–17979 (1994).
54. Perdew, J. P., Burke, K. & Ernzerhof, M. Generalized gradient approximation made simple. *Phys. Rev. Lett.* **77**, 3865–3868 (1996).
55. Perdew, J. P. et al. Atoms, molecules, solids, and surfaces: applications of the generalized gradient approximation for exchange and correlation. *Phys. Rev. B* **46**, 6671–6687 (1992).
56. Becquart, C. S. & Domain, C. Ab initio calculations about intrinsic point defects and He in W. *Nucl. Instrum. Methods Phys. Res. B* **255**, 23–26 (2007).
57. Hou, J. et al. Modification on theory of sink strength: an object kinetic Monte Carlo study. *Comput. Mater. Sci.* **123**, 148–157 (2016).
58. Hou, J. et al. Hydrogen bubble nucleation by self-clustering: density functional theory and statistical model studies using tungsten as a model system. *Nucl. Fusion* **58**, 096021 (2018).
59. Li, Y. G. et al. IM3D: a parallel Monte Carlo code for efficient simulations of primary radiation displacements and damage in 3D geometry. *Sci. Rep.* **5**,18130 (2015).